arXiv:1612.04055v2 [cond-mat.quant-gas] 19 Apr 2017

Negative-Mass Hydrodynamics in a Spin-Orbit–Coupled Bose-Einstein Condensate

M. A. Khamehchi,[1] Khalid Hossain,[1] M. E. Mossman,[1] Yongping Zhang,[2,3,*]
Th. Busch,[2,†] Michael McNeil Forbes,[1,4,‡] and P. Engels[1,§]

[1]*Department of Physics and Astronomy, Washington State University,Pullman, WA 99164, USA*
[2]*Quantum Systems Unit, OIST Graduate University,Onna, Okinawa 904-0495, Japan*
[3]*Department of Physics, Shanghai University,Shanghai 200444, China*
[4]*Department of Physics, University of Washington,Seattle, WA 98105, USA*

A negative effective mass can be realized in quantum systems by engineering the dispersion relation. A powerful method is provided by spin-orbit coupling, which is currently at the center of intense research efforts. Here we measure an expanding spin-orbit coupled Bose-Einstein condensate whose dispersion features a region of negative effective mass. We observe a range of dynamical phenomena, including the breaking of parity and of Galilean covariance, dynamical instabilities, and self-trapping. The experimental findings are reproduced by a single-band Gross-Pitaevskii simulation, demonstrating that the emerging features – shockwaves, soliton trains, self-trapping, etc. – originate from a modified dispersion. Our work also sheds new light on related phenomena in optical lattices, where the underlying periodic structure often complicates their interpretation.

Newton's laws dictate that objects accelerate in proportion to the applied force. An object's mass is generally positive, and the acceleration is thus in the same direction as the force. In some systems, however, one finds that objects can accelerate *against* the applied force, realizing a *negative* effective mass related to a negative curvature of the underlying dispersion relation. Dispersions with negative curvature are playing an increasingly important role in quantum hydrodynamics, fluid dynamics, and optics [1–8]. Superfluid Bose-Einstein condensates (BECs) provide a particularly lucrative playground to investigate this effect, due to their high reproducibility, tunability, and parametric control. In this Letter we report on the experimental observation of negative-mass dynamics in a spin-orbit coupled (SOC) BEC. Modeling the experiments with a single-band Gross-Pitaevskii equation (GPE), we clarify the underlying role of the dispersion relation.

We engineer a dispersion by exploiting Raman dressing techniques that lead to a SOC BEC [9–18]. The presence of the Raman coupling, which acts as an effective perpendicular Zeeman field, opens a gap at the crossing of two separated parabolic free-particle dispersion curves. For suitable parameters, the lower dispersion branch acquires a double-well structure as a function of quasimomentum with a region of negative curvature [see Fig. 1(a)]. In our experiments, the BEC is initially spatially well confined, then allowed to expand in one dimension in the presence of 1D spin-orbit coupling. We observe exceptionally rich dynamics, including the breaking of Galilean covariance, which directly manifests as an anisotropic expansion of the symmetric initial state [see Fig. 1(b)]. As their quasimomentum increases, atoms on one side enter the negative-mass regime and slow down, demonstrating a self-trapping effect. Related to the onset of the negative effective mass are a limiting group velocity and a dynamical instability [19–21] that leads to the formation of shockwaves and solitons.

Our results suggest that a modified dispersion and the corresponding negative effective mass also underlie various "self-trapping" effects seen in optical lattice experiments [22–26]. However, in optical lattices, the origin of the self-trapping effect has been the subject of some controversy due to the occurrence of the underlying periodic potential. This complication is absent on our work.

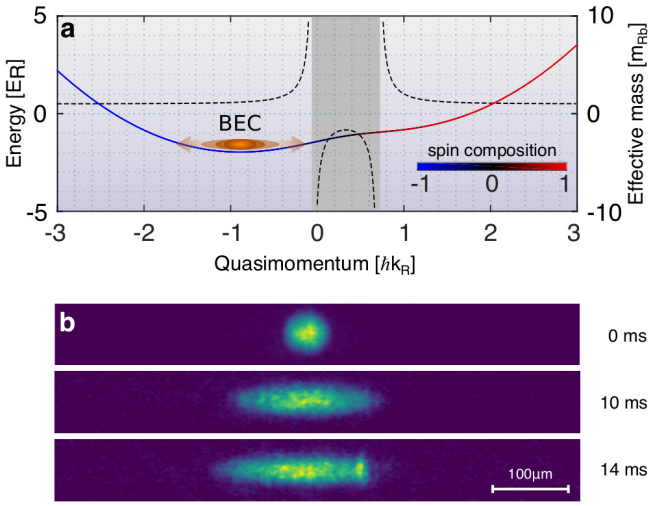


FIG. 1. (a) Schematic representation of the 1D expansion of a SOC BEC. The asymmetry of the dispersion relation (solid curve) causes an asymmetric expansion of the condensate due to the variation of the effective mass. The dashed lines indicate the effective mass, and the shaded area indicates the region of negative effective mass. The parameters used for calculating the dispersion are $\Omega = 2.5E_R$ and $\delta = 1.36E_R$. The color gradient in the dispersion shows the spin polarization of the state. (b) Experimental ToF images of the effectively 1D expanding SOC BEC for expansion times of 0, 10 and 14 ms.

We start with a BEC of approximately 10^5 ^{87}Rb atoms confined in a cigar-shaped trap oriented along the x axis of a far-detuned crossed dipole trap (see [27] for details). A spin-orbit coupling is induced along the x axis by two Raman laser beams that coherently couple atoms in the

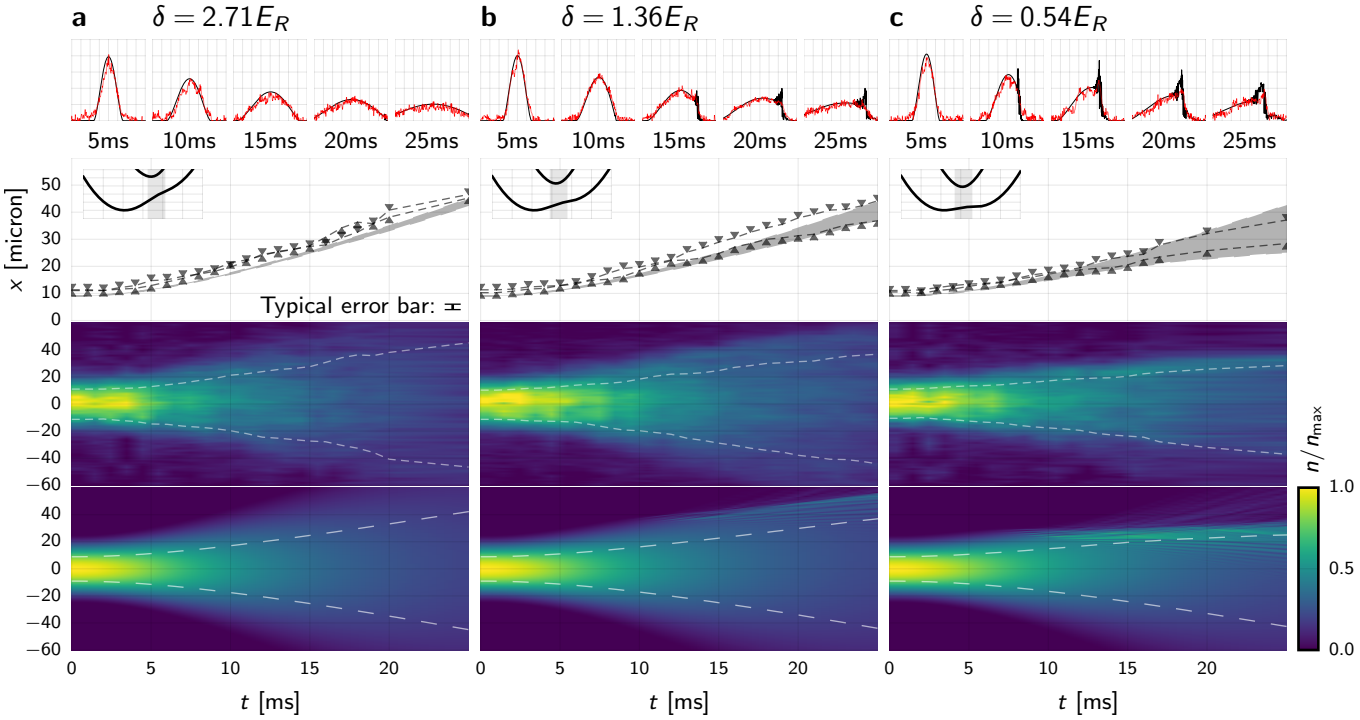


FIG. 2. Anisotropic expansion of a BEC along the direction of spin-orbit coupling (x axis) with the Raman coupling strength $\Omega = 2.5E_R$, and various detunings of (a) $\delta = 2.71E_R$, (b) $\delta = 1.36E_R$, and (c) $\delta = 0.54E_R$, from left to right respectively. The first row shows the experimental integrated cross section of the condensate (dotted red curves) overlaid with results from the GPE simulation (solid black curves). The second row plots the location of the 20% and 80% quantiles with respect to the initial cloud center. The shaded regions present the GPE simulations, while the data points (and dotted lines to guide the eye) are the experimental measurements smoothed slightly by averaging the nearest 3 times. Error estimates are the standard deviation of 5 samples and are comparable with about twice the camera pixel resolution. The insets show the dispersion relation, with the region of negative effective mass lightly shaded. The bottom two rows show the evolution of the expanding condensate from the experiment (upper) and corresponding single-band axially symmetric 3D GPE simulations (lower). The dashed white lines depict the quantiles from the plot above. All experimental data presented here are from *in situ* imaging.

$|F, m_F\rangle = |1, -1\rangle$ and $|1, 0\rangle$ states. A quadratic Zeeman shift effectively decouples the $|1, +1\rangle$ state from the Raman dressing, resulting in a system with pseudo-spin $\frac{1}{2}$ where we identify $|\uparrow\rangle = |1, -1\rangle$ and $|\downarrow\rangle = |1, 0\rangle$. In this system, energy and momentum are characterized in units of $E_R = \hbar^2 k_R^2/2m \approx 2\pi\hbar \times 1843\,\text{Hz}$ and $k_R = 2\pi/\sqrt{2}\lambda_R$, respectively, where $\lambda_R = 789.1\,\text{nm}$.

Using an adiabatic loading procedure, the BEC is initially prepared such that it occupies the lowest minimum of the lower SOC band shown schematically in Fig. 1(a). By suddenly switching off one of the two dipole trap beams, the condensate is allowed to spread out along the x axis. After various expansion times, the BEC is imaged *in situ* (see Fig. 2 and [27]), or after 13 ms of free expansion without a trapping potential or SOC [see Fig. 1(b)]. In the negative x direction, the BEC encounters an essentially parabolic dispersion, while in the positive x direction, it enters a negative-mass region. This leads to a marked asymmetry in the expansion.

Experimental results together with matching numerical simulations are presented in Fig. 2, which shows three sets of data with Raman coupling strength $\Omega = 2.5E_R$ and Raman detunings $\delta \in \{2.71E_R, 1.36E_R, 0.54E_R\}$. With decreasing δ, the dispersion relation (shown in the inset in the second row) develops a more pronounced double-well structure in the lower band. The BEC is initially placed at the global minimum of the lower band, and the expansion dynamics are initiated at time $t = 0$. Integrated cross sections are shown in the first row, the location of the 20% and 80% quantiles in second row, and the experimental and numerical time-slice plots in the third and fourth rows respectively. For $\delta = 2.71E_R$, the expansion is almost symmetric. For $\delta = 1.36E_R$, one sees a noticeable slowing down of the positive edge of the cloud. In the corresponding GPE simulations this occurs at about 11 ms when this edge of the cloud has expanded to 40 µm and the quasimomenta enter the negative-mass region. Here one sees a pileup of the density and a dynamic instability, i.e. an exponential growth in the amplitude of phonon modes. For the smallest detuning

$\delta = 0.54E_R$, the effect is even more pronounced, and in the corresponding GPE simulations, the pileup and instability start sooner at about 8 ms and 25 µm.

At the lowest Raman detuning ($\delta = 0.54E_R$), the experiments show a slowdown at approximately 15 ms in the negative edge, which is not seen in the GPE simulations. We speculate that this is due to finite temperature allowing a population in the second local minimum, requiring more sophisticated simulations (see e.g. [28]). Aside from this effect, we see good agreement between the experiment and zero-temperature GPE simulations, as is expected due to the sizable roton gap (hence small noncondensed fraction [29]) and weak interactions [30].

This justifies the description of the dynamics with a coupled set of GPEs describing the two spin components:

$$\mathrm{i}\hbar\frac{\partial}{\partial t}\begin{pmatrix}|\uparrow\rangle\\|\downarrow\rangle\end{pmatrix} = \begin{pmatrix}\frac{\widehat{\boldsymbol{p}}^2}{2m}+V_\uparrow & \frac{\Omega}{2}e^{2\mathrm{i}k_Rx}\\ \frac{\Omega}{2}e^{-2\mathrm{i}k_Rx} & \frac{\widehat{\boldsymbol{p}}^2}{2m}+V_\downarrow\end{pmatrix}\cdot\begin{pmatrix}|\uparrow\rangle\\|\downarrow\rangle\end{pmatrix}, \tag{1a}$$

$$V_{\uparrow/\downarrow} = -\mu \pm \frac{\delta}{2} + g_{\uparrow\uparrow/\uparrow\downarrow}n_\uparrow + g_{\uparrow\downarrow/\downarrow\downarrow}n_\downarrow \tag{1b}$$

where $\widehat{\boldsymbol{p}} = -\mathrm{i}\hbar\vec{\boldsymbol{\nabla}}$ is the momentum operator, μ is a common chemical potential, k_R is the Raman wave vector, $g_{ab} = 4\pi\hbar^2 a_{ab}/m$, and a_{ab} are the S-wave scattering lengths. For the $|\uparrow\rangle = |1,-1\rangle$ and $|\downarrow\rangle = |1,0\rangle$ hyperfine states of ^{87}Rb, the scattering lengths are almost equal and for our numerics we take $a_{\uparrow\uparrow} = a_{\uparrow\downarrow} = a_{\downarrow\downarrow} = a_s$. We compare our experimental results with 3D axially symmetric simulations for $\omega_\perp = 2\pi \times 162\,\mathrm{Hz}$ and realistic experimental parameters.

One of the theoretical results we wish to convey is that in many cases (e.g., Refs. [32, 33]), a single-band model can capture the essential dynamics with modified dispersion:

$$\mathrm{i}\hbar\frac{\partial}{\partial t}|\psi\rangle = [E_-(\widehat{\boldsymbol{p}}) + gn + V_{\mathrm{ext}}(x)]\,|\psi\rangle \tag{2}$$

where $E_-(\widehat{\boldsymbol{p}})$ is the dispersion of the lower band obtained by diagonalizing Eq. (1) for homogeneous states. For inhomogeneous densities this picture is locally valid for slowly varying densities, similar to the Thomas-Fermi approximation, and remains valid as long as the system is gently excited compared to the band separation, which is proportional to the strength Ω of the Raman coupling. With our parameters, the single-band model exhibits almost identical results to the multiband description, quantitatively reproducing many aspects of the experiment. The approximate equality of the coupling constants allows one to define a spin-quasimomentum mapping that relates the two-component spin populations $n_\uparrow$ and $n_\downarrow$ to the quasimomentum q of the single-component state:

$$\frac{n_\downarrow - n_\uparrow}{n_\downarrow + n_\uparrow} = \frac{k-d}{\sqrt{(k-d)^2+w^2}}, \tag{3}$$

where we have defined the dimensionless parameters $k = p/\hbar k_R$, $d = \delta/4E_R$, and $w = \Omega/4E_R$. Our simulations solve this model with a discrete variable representation (DVR) basis (see, e.g., Ref. [34]) with 4096×128 lattice points in a periodic tube of length 276 µm and radius 10.8 µm. This greatly simplified analysis shows that all of the interesting phenomena observed in the experiment – asymmetric expansion, the pileup, slowing down, and instabilities – follow from the modified dispersion relationship.

Having introduced the single-component theory, we now derive the hydrodynamics of this model by effecting a Madelung transformation $\psi = \sqrt{n}e^{\mathrm{i}\phi}$ where $n(\vec{\boldsymbol{x}},t) = n_\uparrow + n_\downarrow$ is the total density at position $\vec{\boldsymbol{x}}$ and time t, and the phase $\phi(\vec{\boldsymbol{x}},t)$ acts as a quasimomentum potential $\vec{\boldsymbol{p}} = \hbar\vec{\boldsymbol{\nabla}}\phi$. The hydrodynamic equations are

$$\frac{\partial}{\partial t}n + \vec{\boldsymbol{\nabla}}\cdot(n\vec{\boldsymbol{v}}) = 0, \tag{4a}$$

$$\frac{\partial\vec{\boldsymbol{v}}_*}{\partial t} + (\vec{\boldsymbol{v}}_*\cdot\vec{\boldsymbol{\nabla}})\vec{\boldsymbol{v}}_* = \boldsymbol{M}_*^{-1}\cdot(\overbrace{-\vec{\boldsymbol{\nabla}}[V_{\mathrm{eff}}+V_Q]}^{\vec{\boldsymbol{F}}}), \tag{4b}$$

$$[\boldsymbol{M}_*^{-1}]_{ij} = \frac{\partial E_-(\vec{\boldsymbol{p}})}{\partial p_i\partial p_j}, \qquad [\vec{\boldsymbol{v}}_*]_i = \frac{\partial E_-(\vec{\boldsymbol{p}})}{\partial p_i}, \tag{4c}$$

where $\vec{\boldsymbol{v}}$ is the group velocity and $\vec{\boldsymbol{j}} = \vec{\boldsymbol{v}}n$ is the current density. $V_{\mathrm{eff}} = V_{\mathrm{ext}}(\vec{\boldsymbol{x}},t) + gn(\vec{\boldsymbol{x}},t)$ is the effective potential, including both the external potential and mean-field effects. What differs from the usual Madelung equations is that third and higher derivatives of the dispersion $E_-(\vec{\boldsymbol{p}})$ affect the velocity $\vec{\boldsymbol{v}}_*$ and quantum potential $V_Q(n,\vec{\boldsymbol{p}})$. While for homogeneous matter, $\vec{\boldsymbol{v}} = \vec{\boldsymbol{v}}_*$, this relationship is broken in inhomogeneous matter and the quantum potential acquires terms beyond the usual quantum pressure term $V_Q(n) \propto \nabla^2\sqrt{n}/\sqrt{n}$. For approximately homogeneous sections of the cloud, however, these corrections are small: $\vec{\boldsymbol{v}} \approx \vec{\boldsymbol{v}}_*$ and the usual hydrodynamic behavior is realized. In particular, $\partial\vec{\boldsymbol{v}}/\partial t \approx \boldsymbol{M}_*^{-1}\cdot\vec{\boldsymbol{F}}$, so that the group velocity responds classically, accelerating against the force $\vec{\boldsymbol{F}}$ if the effective mass is negative. The experiment may be qualitatively explained using a Thomas-Fermi–like approximation where each point of the cloud is locally described by a plane-wave with local quasimomentum p. Initially, equilibrium is established between the external trapping force $-\nabla V_{\mathrm{ext}}$ and the internal mean-field pressure $-\nabla(gn)$, with the quasimomentum $p = p_0$ minimizing the kinetic energy $E'_-(p_0) = 0$. About this minimum, the effective mass is positive, so once the trapping potential V_{ext} is reduced, the cloud starts to expand due to the mean-field pressure, generating an outward group velocity and quasimomenta. As the quasimomentum along the positive x-axis approaches the negative-mass region (see Fig. 3), the acceleration slows significantly compared with the acceleration along the negative axis, leading to the asymmetric expansion seen in Fig. 2: a manifestation of the broken

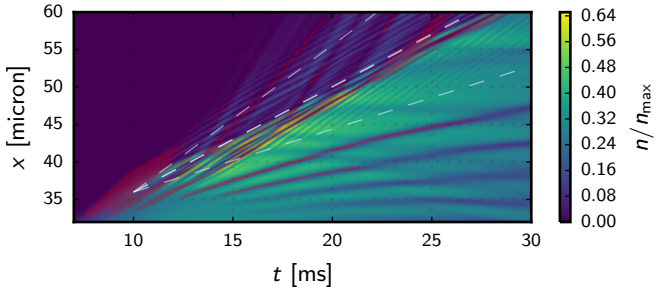


FIG. 3. Zoom of a 1D simulation matching the lower middle frame of Fig. 2 showing the total density $n = n_\uparrow + n_\downarrow$ as a function of time in the region where the dynamic instability first appears. Dashed lines are the three group velocities $v_g = E'_-(k)$ at the quasimomenta k where the inverse effective mass $m_*^{-1} = E''_-(k)$ first becomes negative (steepest line), the point of maximum m_*^{-1} (middle), and the point where the m_*^{-1} returns to positive (least steep line). Red points demonstrate where the local quasimomentum lies in the negative-mass region. Note that, as described in the text, the pileup initially contains many density fluctuations, but sharpens as solitons and phonons "radiate" energy away from the wall.

Galilean covariance and parity in SOC systems. Once the quasimomentum enters the negative-mass region, the acceleration opposes the force, and the cloud experiences the "self-trapping" effect where the positive mean-field pressure tends to prevent further expansion.

A similar effect has been reported in optical lattices near the edge of the Brillouin zone [22, 23, 35]. These "self-trapping" effects in lattices have been attributed to several different phenomena. One, based on a Josephson effect with suppressed tunneling between neighboring sites [23, 32], was predicted from a variational framework [36]. Another explanation is that the sharp boundary is a "gap soliton" [37], though this explanation is disputed by [32] on the basis that solitons should remain stable whereas the latter observe self-trapping only for a finite period of time. Finally, self-trapping has been explained in terms of the Peierls-Nabarro energy barrier [38]. In all of these cases, the self-trapping occurs where the effective mass becomes negative, but the interpretation of the self-trapping effect in optical lattices is complicated by the presence of spatial modulations in the potential.

The beauty of engineering dispersions with SOC BECs is that lattice complications are removed. The success of the single-band model in reproducing the experiment demonstrates clearly that the self-trapping results from the effective dispersion relationship. A single-band model using the dispersion of the lowest band in an optical lattice is able to explain the previous observation of self-trapping in lattice systems, clearly demonstrating the importance of the band structure and deemphasizing the role of the underlying lattice geometry of coupled wells. This result is confirmed by using a tight-binding approximation to map the optical lattice of Ref. [32] to a single band model, which reproduces their results. In our simulations, although the boundary appears to be very stable, it is "leaky". This can be seen from Fig. 3 where the boundary maintains its shape, but permits a small number of fast moving particles to escape. Similarly, in optical lattice systems such fast moving particles are responsible for the continued increase in the width of the cloud seen by [32] even though the boundary remains stopped. This may resolve the apparent discrepancy between [32] and [37] as a quasistable but leaky gap soliton.

What sets the limiting velocity of the expanding edge? In the optical lattice system of Ref. [22], the limiting velocity was observed to lie at the inflection point where the mass first starts to become negative. In contrast, our GPE simulations for SOC BECs clearly show this limiting velocity to lie fully inside the negative-mass region, near the point of maximum negative acceleration (maximum negative inverse effective mass) (see Fig. 3). While this qualitatively describes the limiting velocity, the full effect is somewhat subtle. The limiting velocity ultimately depends on several factors, including the preparation of the system [39]. It requires a quasistable boundary which is tied to the negative effective mass through a dynamical instability. From the GPE simulations, the picture emerges that once the cloud enters the negative-mass region, small fluctuations grow exponentially forming the sharp boundary of the cloud. Initially these growing modes appear chaotic, but as is typical with dispersive shock-waves (see [40] and references therein), energy is "radiated" from the boundary in the form of phonons and soliton trains that are clearly visible in Fig. 3. As energy is dissipated, the boundary appears to sharpen due to nonlinear effects. This seems critically connected to the negative effective mass as a similar boundary with positive mass dispersion broadens [39].

In conclusion, we have studied negative-mass hydrodynamics both experimentally and theoretically in an expanding spin-orbit coupled Bose-Einstein condensate. The experimental results are quantitatively reproduced with an effective single-band zero-temperature GPE-like model derived from the SOC Hamiltonian. With this model, we see that the pileup and subsequent boundary behavior are intimately related to the presence of a negative effective mass $m_*^{-1} = E''_-(p)$ in the effective dispersion for the band. From linear response theory, one finds a dynamical instability closely associated with the negative effective mass that leads to the sudden increase in density. The boundary clearly demonstrates radiation of phonons and soliton trains, which appear to remove energy from the region, thereby allowing the boundary to stabilize. The stability of the boundary and its final velocity depend critically on the existence of a negative effective mass. With this work, we have also clarified the interpretation of self-trapping phenomena observed in optical lattices [23, 32], demonstrating that this is nat-

urally explained by a negative effective mass. Spin-orbit coupling provides a powerful tool for engineering the dispersion $E_{-}(p)$ without the additional complications of spatial modulations that appear in the context of optical lattices.

Acknowledgements: We thank Mark Hoefer for useful discussions. This work was supported in part by a Washington State University (WSU) New Faculty Seed Grant, and the Okinawa Institute of Science and Technology Graduate University. P. E. acknowledges funding from the National Science Foundation (NSF) under grant No. PHY-1607495. Y. Z. is supported in part by the Thousand Young Talent Program of China, and the Eastern Scholar Program of Shanghai.

REFERENCES

[1] M. A. H. Tucker and A. F. G. Wyatt, "Direct evidence for r^{-} rotons having antiparallel momentum and velocity," Science **283**, 1150–1152 (1999).

[2] Nicholas K. Lowman and M. A. Hoefer, "Dispersive shock waves in viscously deformable media," J. Fluid Mech. **718**, 524–557 (2013).

[3] Matteo Conforti and Stefano Trillo, "Dispersive wave emission from wave breaking," Opt. Lett. **38**, 3815–3818 (2013).

[4] Matteo Conforti, Fabio Baronio, and Stefano Trillo, "Resonant radiation shed by dispersive shock waves," Phys. Rev. A **89**, 013807 (2014).

[5] Matteo Conforti and Stefano Trillo, "Radiative effects driven by shock waves in cavity-less four-wave mixing combs," Opt. Lett. **39**, 5760–5763 (2014).

[6] Stefania Malaguti, Matteo Conforti, and Stefano Trillo, "Dispersive radiation induced by shock waves in passive resonators," Opt. Lett. **39**, 5626–5629 (2014).

[7] Matteo Conforti, Stefano Trillo, Arnaud Mussot, and Alexandre Kudlinski, "Parametric excitation of multiple resonant radiations from localized wavepackets," Sci. Rep. **5**, 9433 EP – (2015).

[8] Gennady A. El and Noel F. Smyth, "Radiating dispersive shock waves in non-local optical media," Proc. Roy. Soc. (London) A **472**, 20150633 (2016).

[9] Y. J. Lin, K. Jimenez-Garcia, and I. B. Spielman, "Spin-orbit-coupled Bose-Einstein condensates," Nature **471**, 83–86 (2011).

[10] Pengjun Wang, Zeng-Qiang Yu, Zhengkun Fu, Jiao Miao, Lianghui Huang, Shijie Chai, Hui Zhai, and Jing Zhang, "Spin-orbit coupled degenerate fermi gases," Phys. Rev. Lett. **109**, 095301 (2012).

[11] Lawrence W. Cheuk, Ariel T. Sommer, Zoran Hadzibabic, Tarik Yefsah, Waseem S. Bakr, and Martin W. Zwierlein, "Spin-injection spectroscopy of a spin-orbit coupled fermi gas," Phys. Rev. Lett. **109**, 095302 (2012).

[12] Jin-Yi Zhang, Si-Cong Ji, Zhu Chen, Long Zhang, Zhi-Dong Du, Bo Yan, Ge-Sheng Pan, Bo Zhao, You-Jin Deng, Hui Zhai, Shuai Chen, and Jian-Wei Pan, "Collective dipole oscillations of a spin-orbit coupled Bose-Einstein condensate," Phys. Rev. Lett. **109**, 115301 (2012).

[13] Chunlei Qu, Chris Hamner, Ming Gong, Chuanwei Zhang, and Peter Engels, "Observation of *Zitterbewegung* in a spin-orbit-coupled Bose-Einstein condensate," Phys. Rev. A **88**, 021604 (2013).

[14] Abraham J. Olson, Su-Ju Wang, Robert J. Niffenegger, Chuan-Hsun Li, Chris H. Greene, and Yong P. Chen, "Tunable landau-zener transitions in a spin-orbit-coupled Bose-Einstein condensate," Phys. Rev. A **90**, 013616 (2014).

[15] C. Hamner, Yongping Zhang, M. A. Khamehchi, Matthew J. Davis, and P. Engels, "Spin-orbit-coupled Bose-Einstein condensates in a one-dimensional optical lattice," Phys. Rev. Lett. **114**, 070401 (2015).

[16] Xinyu Luo, Lingna Wu, Ruquan Wang, and L You, "Atomic spin orbit coupling synthesized with gradient magnetic fields," J. Phys.: Conf. Ser. **635**, 012013 (2015); Xinyu Luo, Lingna Wu, Jiyao Chen, Qing Guan, Kuiyi Gao, Zhi-Fang Xu, L. You, and Ruquan Wang, "Tunable atomic spin-orbit coupling synthesized with a modulating gradient magnetic field," Scientific Reports **6**, 18983 (2016).

[17] Lianghui Huang, Zengming Meng, Pengjun Wang, Peng Peng, Shao-Liang Zhang, Liangchao Chen, Donghao Li, Qi Zhou, and Jing Zhang, "Experimental realization of two-dimensional synthetic spin-orbit coupling in ultracold fermi gases," Nat. Phys. **12**, 540–544 (2016).

[18] Zhan Wu, Long Zhang, Wei Sun, Xiao-Tian Xu, Bao-Zong Wang, Si-Cong Ji, Youjin Deng, Shuai Chen, Xiong-Jun Liu, and Jian-Wei Pan, "Realization of Two-Dimensional Spin-orbit Coupling for Bose-Einstein Condensates," (2015), arXiv:1511.08170.

[19] L. Fallani, L. De Sarlo, J. E. Lye, M. Modugno, R. Saers, C. Fort, and M. Inguscio, "Observation of dynamical instability for a Bose-Einstein condensate in a moving 1d optical lattice," Phys. Rev. Lett. **93**, 140406 (2004), arXiv:cond-mat/0404045.

[20] Immanuel Bloch, "Ultracold quantum gases in optical lattices," Nat. Phys. **1**, 23–30 (2005).

[21] Ishfaq Ahmad Bhat, T. Mithun, B. A. Malomed, and K. Porsezian, "Modulational instability in binary spin-orbit-coupled bose-einstein condensates," Phys. Rev. A **92**, 063606 (2015).

[22] B. Eiermann, P. Treutlein, Th. Anker, M. Albiez, M. Taglieber, K.-P. Marzlin, and M. K. Oberthaler, "Dispersion management for atomic matter waves," Phys. Rev. Lett. **91**, 060402 (2003).

[23] Th. Anker, M. Albiez, R. Gati, S. Hunsmann, B. Eiermann, A. Trombettoni, and M. K. Oberthaler, "Nonlinear self-trapping of matter waves in periodic potentials," Phys. Rev. Lett. **94**, 020403 (2005).

[24] K. Henderson, H. Kelkar, B. Gutiérrez-Medina, T. C. Li, and M. G. Raizen, "Experimental study of the role of atomic interactions on quantum transport," Phys. Rev. Lett. **96**, 150401 (2006).

[25] Aaron Reinhard, Jean-Félix Riou, Laura A. Zundel, David S. Weiss, Shuming Li, Ana Maria Rey, and Rafael Hipolito, "Self-trapping in an array of coupled 1d Bose gases," Phys. Rev. Lett. **110**, 033001 (2013).

[26] J. P. Ronzheimer, M. Schreiber, S. Braun, S. S. Hodgman, S. Langer, I. P. McCulloch, F. Heidrich-Meisner, I. Bloch, and U. Schneider, "Expansion dynamics of in-

teracting bosons in homogeneous lattices in one and two dimensions," Phys. Rev. Lett. **110**, 205301 (2013).

[27] See Supplemental Material at [URL will be inserted by publisher] for high-resolution images and details about the experimental preparation and analysis.

[28] A. Minguzzi, S. Succi, F. Toschi, M. P. Tosi, and P. Vignolo, "Numerical methods for atomic quantum gases with applications to bose–einstein condensates and to ultracold fermions," Phys. Rep. **395**, 223–355 (2004); Nick P. Proukakis, Simon A. Gardiner, Matthew J. Davis, and Marzena Szymanska, eds., *Quantum Gases: Finite Temperature and Non-Equilibrium Dynamics*, Cold Atoms, Vol. 1 (Imperial College Press, London, 2013).

[29] Yi-Cai Zhang, Zeng-Qiang Yu, Tai Kai Ng, Shizhong Zhang, Lev Pitaevskii, and Sandro Stringari, "Superfluid Density of a Spin-orbit Coupled Bose Gas," Phys. Rev. A **94**, 033635 (2016), arXiv:1605.02136.

[30] The scattering lengths are $a_{\uparrow\uparrow} = 100.40a_0$, $a_{\downarrow\downarrow} = 100.86a_0$, and $a_{\uparrow\downarrow} = 100.41a_0$ [31], so that the dimensionless gas parameter $na^3 < 3 \times 10^{-5} \ll 10^{-3}$.

[31] S. J. J. M. F. Kokkelmans, (private communication); B. J. Verhaar, E. G. M. van Kempen, and S. J. J. M. F. Kokkelmans, "Predicting scattering properties of ultracold atoms: Adiabatic accumulated phase method and mass scaling," Phys. Rev. A **79**, 032711 (2009).

[32] Bingbing Wang, Panming Fu, Jie Liu, and Biao Wu, "Self-trapping of Bose-Einstein condensates in optical lattices," Phys. Rev. A **74**, 063610 (2006).

[33] Yan Li, Chunlei Qu, Yongsheng Zhang, and Chuanwei Zhang, "Dynamical spin-density waves in a spin-orbit-coupled Bose-Einstein condensate," Phys. Rev. A **92**, 013635 (2015).

[34] Robert G. Littlejohn and Matthew Cargo, "Bessel discrete variable representation bases," J. Chem. Phys. **117**, 27–36 (2002).

[35] Rockson Chang, Shreyas Potnis, Ramon Ramos, Chao Zhuang, Matin Hallaji, Alex Hayat, Federico Duque-Gomez, J. E. Sipe, and Aephraim M. Steinberg, "Observing the onset of effective mass," Phys. Rev. Lett. **112**, 170404 (2014).

[36] Andrea Trombettoni and Augusto Smerzi, "Discrete solitons and breathers with dilute Bose-Einstein condensates," Phys. Rev. Lett. **86**, 2353–2356 (2001).

[37] Tristram J. Alexander, Elena A. Ostrovskaya, and Yuri S. Kivshar, "Self-trapped nonlinear matter waves in periodic potentials," Phys. Rev. Lett. **96**, 040401 (2006).

[38] H. Hennig, T. Neff, and R. Fleischmann, "Dynamical phase diagram of gaussian wave packets in optical lattices," Phys. Rev. E **93**, 032219 (2016).

[39] Edward Delikatney, Khalid Hossain, and Michael McNeil Forbes, in preperation.

[40] G. A. El and M. A. Hoefer, "Dispersive shock waves and modulation theory," Physica D: Nonlinear Phenomena **333**, 11–65 (2016), arXiv:1602.06163

NUMERICAL SIMULATIONS

In principle, since the trap is highly elongated, one can use an effective 1D simulation by tuning the coupling constants appropriately as described in [41, 42]. For the experimental parameters, this effective 1D approximation works quite well, but since there are some radial excitations, we compare directly with 3D axially symmetric simulation with $\omega_\perp = 2\pi \times 162\,\mathrm{Hz}$. Our simulations are performed using an axially symmetric DVR basis (see e.g. [34]) with 4096×128 lattice points in a periodic tube of length 276 µm and radius 10.8 µm.

In Fig. 4 we compare the single-band model (2) to the full two-component model (1), demonstrating that for the experiment under consideration, all the relevant phenomena result purely from the modified dispersion relationship $E_-(\widehat{\boldsymbol{p}})$. Even when studying systems with significant population of the upper band such as the dynamical spin-density waves demonstrated in [33], we find that the single-component model (2) captures most of the bulk effects: i.e. it correctly models the dynamical behavior of the total density $n_\uparrow + n_\downarrow$, but the significant population of the upper branch breaks the spin-quasimomentum mapping (3). In this figure we also compare 3D axially-symmetric simulations with 1D simulation where we have tuned the coupling constant using the relationship in [41]. This comparison demonstrates that, while the 1D simulations qualitatively match the experiments, they exhibit some quantitative differences with the 3D simulations.

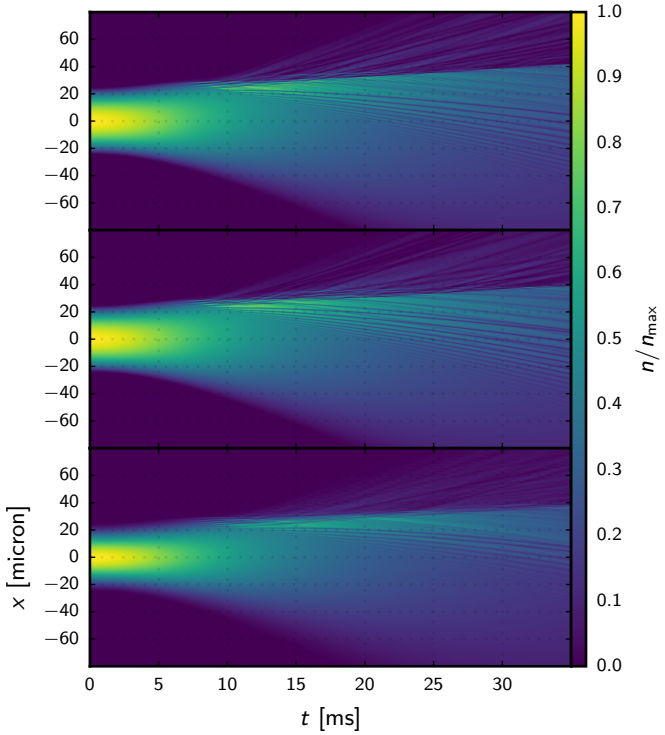


FIG. 4. **Comparison between simulations.** Comparison of the full two-component 1D GPE model (1) (top) with the 1D single-band model (2) (middle) and the axially symmetric 3D single-band model (bottom) for detuning $\delta = 0.54E_R$ and Raman coupling strength $\Omega = 2.5E_R$.

Our simulations here explore only the dynamics of the condensate. Extensions to the GPEs (see e.g. [28] for reviews) are require to capture the dynamics of the non-condensed fraction due to finite temperature, and quantum fluctuations, but are beyond the score of the present work. (For example, a significant non-condensed fraction is expected when the gap in the roton branch vanishes [29]. For our parameters, the roton branch still has a large gap.) The deviations described in the text between GPE simulations and experiment at the lowest Raman detuning will provide a way to test these extensions.

EXPERIMENTAL METHODS

The experiment begins with approximately 10^5 ^{87}Rb atoms confined by two trapping dipole beams which together produce harmonic trapping frequencies of $(\omega_x, \omega_y, \omega_z) = 2\pi\times(26,\ 170 \text{ and } 154)\,\mathrm{Hz}$. SOC is then generated along the x-axis by two perpendicular Raman beams of wavelength $\lambda_R = 789.1\,\mathrm{nm}$ [see Fig. 5(a)]. The Raman beams coherently couple the $|F,\ m_F\rangle = |1,-1\rangle$ and $|1,0\rangle$ states. A homogeneous bias field of $B \approx 10\,\mathrm{G}$ is applied along the x-axis, leading to a Zeeman splitting of the atomic levels. The quadratic Zeeman shift of $7.8E_R$ effectively decouples the $|1,+1\rangle$ state from the Raman dressing, resulting in a system with pseudospin $\frac{1}{2}$ where we identify $|\uparrow\rangle = |1,-1\rangle$ and $|\downarrow\rangle = |1,0\rangle$ [see Fig. 5(b)]. After the atoms are dressed by the Raman beams with a specific Raman coupling strength

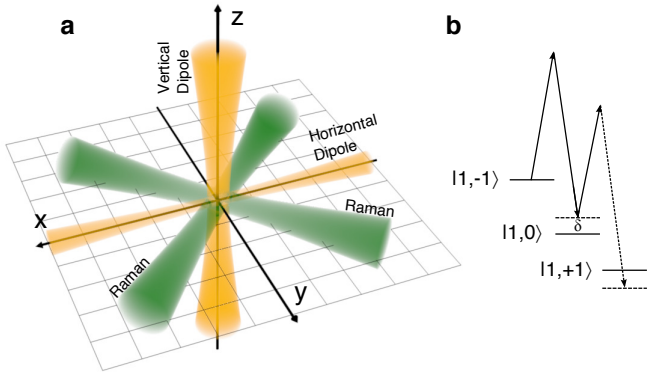


FIG. 5. (a) Experimental arrangement of the trap (yellow) and the Raman (green) beams. The angle between the Raman beams is 90°. (b) Raman coupling scheme in the $F = 1$ manifold. The $|1,+1\rangle$ state is effectively decoupled due to the quadratic Zeeman shift induced by an external bias field along the x direction.

Ω and detuning δ, the vertical dipole beam is rapidly switched off, reducing the confinement along the x-axis from $\omega_x = 2\pi\times 26$ Hz to $\omega_x = 2\pi\times 1.4$ Hz. This allows the SOC BEC to expand along the direction of the spin-orbit coupling, revealing the rich dynamics discussed in the main text. The extent of the cloud as depicted in Fig. 2 is taken from in-trap images. Figure 1(b) depicts experimental images taken after an in-trap expansion time denoted to the left of the image, followed by 13 ms free expansion.

COMPARISON

To supplement the comparison between the numerical and experimental results, we include in Fig. 6 a high-resolution comparison between the numerical and experimental *in situ* images. Note that we have not added noise or pixel averaging effects to the numerical simulations so that underlying features (solitons etc.) remain unobscured.

SUPPLEMENTARY REFERENCES

[41] M. Olshanii, Phys. Rev. Lett. **81**, 938 (1998), URL `http://link.aps.org/doi/10.1103/PhysRevLett.81.938`.

[42] Y.-C. Zhang, S.-W. Song, and W.-M. Liu, Sci. Rep. **4**, 4992 (2014), URL `http://www.ncbi.nlm.nih.gov/pmc/articles/PMC4034008/`.

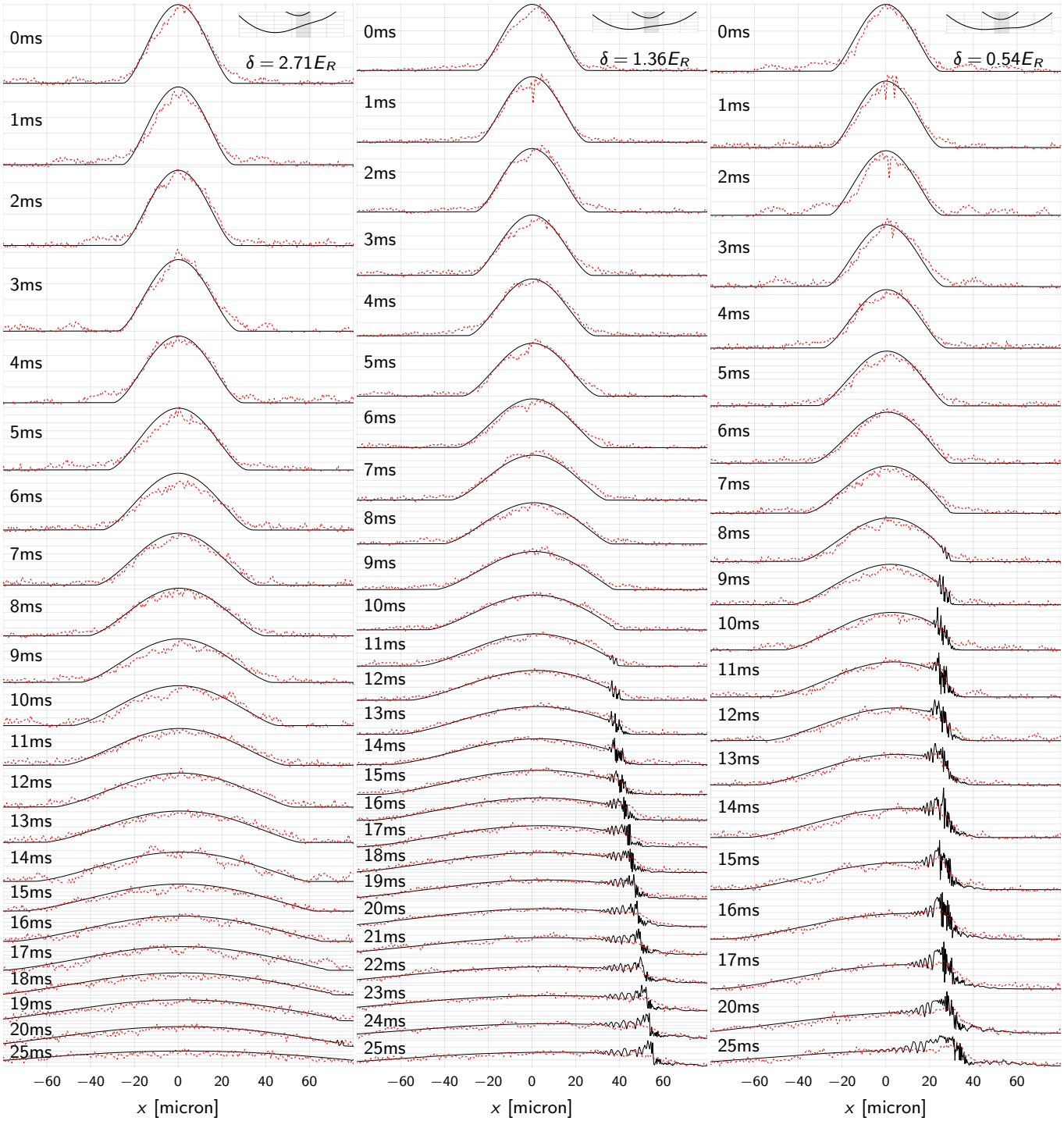


FIG. 6. **In-situ data: Experiment and Theory.** In-situ experimental integrated cross section of the condensate (dotted red curves) overlaid with results from the axially symmetric single-band 3D GPE simulations (solid black curves) with the Raman coupling strength $\Omega = 2.5E_R$, and various detunings of (a) $\delta = 2.71E_R$, (b) $\delta = 1.36E_R$, and (c) $\delta = 0.54E_R$, from left to right respectively. The top insets show the dispersion relation, with the region of negative effective mass lightly shaded.